PHYSICAL REVIEW B **81**, 214106 (2010)

# Interaction of a $\frac{1}{2}\langle 111\rangle$ screw dislocation with Cr precipitates in bcc Fe studied by molecular dynamics

D. Terentyev,[1,*] G. Bonny,[1] C. Domain,[2] and R. C. Pasianot[3,4]
[1]*Nuclear Materials Science Institute, SCK-CEN, Boeretang 200, B-2400 Mol, Belgium*
[2]*Dept. MMC, EDF-R&D, Site des Renardières, F-77218 Moret-sur-Loing, France*
[3]*Depto. de Materiales, CAC-CNEA, Avda. Gral. Paz 1499, San Martín, 1650 Pcia. Buenos Aires, Argentina*
[4]*Depto. de Materiales, CONICET, Avda. Gral. Paz 1499, San Martín, 1650 Pcia. Buenos Aires, Argentina*

(Received 2 December 2009; revised manuscript received 14 April 2010; published 9 June 2010)

The appearance of Cr-rich precipitates ($\alpha'$ prime) after thermal aging or irradiation is a typical feature of high-Cr ferritic/martensitic steels. $\alpha'$ particles, obstructing the motion of dislocations, are long known to be the cause of hardening and embrittlement, observed in steels and Fe-Cr binary alloys. In this work, we consider the interaction of a screw dislocation with Cr precipitates in a bcc Fe matrix using a molecular dynamics technique. We derive an interatomic potential, based on the existing two band formalism, specifically accounting for information about screw dislocation properties in the Fe-Cr system available from the first-principles calculations. The derived potential was accordingly benchmarked and successfully applied to study the interaction of a moving $\frac{1}{2}\langle 111\rangle$ screw dislocation with Cr precipitates. The results obtained suggest that two principally different interaction mechanisms may operate depending on the interatomic potential applied. The improved potential predicts stable glide of a screw dislocation, whereas the potential predicting an incorrect core structure shows the bypass movement of the dislocation around the precipitate without shearing of the latter. The bypass movement involves the glide of the dislocation under the precipitate in the plane inclined to the maximum resolved shear stress plane. The reasons for this were rationalized in terms of the compact-to-degenerate transformation of the structure occurring at the precipitate matrix interface. This study emphasizes the importance of the atomic scale features and dislocation core effects in the process of the interaction of a dislocation with secondary phase particles.

DOI: 10.1103/PhysRevB.81.214106 PACS number(s): 81.40.Cd, 81.40.Ef, 87.10.Tf

## I. INTRODUCTION

The use of high-Cr ferritic/martensitic (FM) steels as structural materials for near future nuclear power systems (generation IV) and fusion reactors, requires the material to keep its properties obeying safety standards during the whole scheduled lifetime. Although, FM steels are chosen to be primary candidates due to their excellent swelling resistance and advanced mechanical properties, they suffer from radiation hardening and embrittlement. One of the reasons for the degradation of mechanical properties of FM steels (at elevated temperature) is $\alpha$-$\alpha'$ phase separation,[1,2] occurring at temperatures below ~600 °C and resulting in the formation of finely dispersed nanometric Cr-rich precipitates. The quantitative understanding of the impact of the $\alpha$-$\alpha'$ phase separation on mechanical properties of FM steels is thus clearly an important issue to be tackled.

According to the conventional phase diagram,[3] binary Fe-Cr alloys exhibit $\alpha$-$\alpha'$ decomposition if the Cr content exceeds ~10%. Recent studies on FM steels of different compositions showed that $\alpha'$ particles form already in 9%Cr steels at 400 °C under thermal aging (for 10 000 h) (Ref. 4) and at 250 °C under irradiation (up to 3 dpa), which significantly accelerates phase separation and results in a high density of Cr precipitates ($\sim 10^{23}$ $\mathrm{m}^{-3}$ with mean size of ~1.5 nm). The presence of the $\alpha'$ particles that obstruct dislocation motion is long known to be the cause of hardening and embrittlement, observed in FM steels and Fe-Cr binary alloys containing more than 12%Cr after thermal aging (so-called "475 °C embrittlement").[1,2]

Nowadays, large scale molecular dynamics (MD) simulations are widely used to investigate details of mechanisms of the interaction of dislocations with different types of defects (i.e., precipitates, voids, dislocation loops, etc.) in a variety of materials (see Ref. 5 for a recent review). In such simulations, the motion of a dislocation is ensured by applying shear strain or stress on the surfaces of an MD cell.[6,7] The critical resolved shear stress can be calculated directly from such simulations at 0 K [molecular statics (MS)] and finite temperature (MD), and the interaction mechanism can be investigated using numerical dislocation core identification techniques coupled with visualization tools.

Cr-rich precipitates, being nearly pure (judging from the phase diagram[3] and relying on the recently obtained results using atomistic modeling[8–10]) are oversized coherent bcc particles with shear modulus higher than the one of Fe or Fe-rich Fe-Cr alloys. Size misfit, modulus misfit, and chemical strengthening effects are expected to be the main mechanisms determining the resistance of Cr-rich precipitates to shear.[11] Recently, however, another type of strengthening effect was found by using MS simulations in bcc Fe. The study of the interaction of a screw dislocation with small bcc Cu precipitates revealed a dislocation core structure modification when the latter penetrates into a precipitate.[12,13] The core modification leads to a substantial increase in the interaction energy between dislocation and precipitate and thus the strength of a precipitate is expected to rise due this transformation.[12,13] However, the observed core modification was attributed to the instability of bcc copper precipitates in Fe.

In the case of FM steels, Cr precipitates are coherent with the Fe-Cr matrix, thus changes in the dislocation core structure are not expected. Recently, the interaction of Cr precipitates with a $\frac{1}{2}\langle 111\rangle$ screw dislocation in an Fe matrix was studied by MS simulations[14] using a two band model potential.[15] The dislocation-precipitate interaction energy was calculated as a function of distance between the dislocation line and precipitate center, imitating the dislocation glide in a $\{110\}$ plane through a regular square array of precipitates. The main contribution to the precipitate-dislocation interaction was determined to come from the shear modulus misfit, whereas chemical strengthening was shown to play a minor role. In addition, a weak attractive interaction between the dislocation and precipitate near the precipitate-matrix interface (PMI) was found, which cannot be explained within the framework of a shear modulus misfit model. The core of the screw dislocation was found to spread significantly over the precipitate surface at the moment the dislocation penetrates the precipitate. However, the bcc structure of the Cr precipitate was found to be stable with respect to the presence of the dislocation inside the precipitate.[11,14] It is important to note that the set of potentials from Ref. 15 predicts an isotropic and threefold degenerate structure of the dislocation core in Fe and Cr, respectively.[14] Correspondingly, the change in the core structure from compact (in the matrix) to degenerate (in the precipitate) occurred for dislocation segments inside the precipitate. The segments located nearby the PMI were seen to acquire an essential edge component.[14] We note, however, that this core structure transformation might also be an artifact of the applied interatomic model.

Indeed, the Cr-Cr potential derived in Ref. 15 predicts the nondegenerate core, while no published density-functional theory (DFT) data on the core structure in pure Cr is available. The atomic-row (AR) method,[16] which accounts for the relaxation between $\langle 111\rangle$ atomic strings and the inter-row potential derived from DFT calculations, suggests that the core structure is nondegenerate just as in pure Fe.[17] Furthermore, the interaction of the $\frac{1}{2}\langle 111\rangle$ screw dislocation with Cr nanoclusters (or rather nanowires) was also studied using the AR model.[17] It was found that the presence of Cr rows in the core of the screw dislocation has almost no effect on the polarization of the dislocation core. The core remains isotropic even if the dislocation is placed in a small Cr cluster made of three $\langle 111\rangle$ Cr rows. The shearing of such a Cr nanowire, however, required application of additional stress calculated to be about 12% higher than the Peierls stress for the screw dislocation in pure Fe (1.6 GPa).[17] In addition, the Peierls stress in pure Cr was found to be ~30% higher than in pure Fe.[17]

Even though the AR model can use a DFT parameterization it has a serious disadvantage. The model accounts only for relaxation along the dislocation line and neglects the edge component or any other strain component that is not aligned with the $\langle 111\rangle$ direction. Therefore such a model neglects any nonscrew component which can be very important in the process of relaxation of the dislocation near the PMI. In addition, in Ref. 17 such a model was used to consider nanowires of Cr rather than realistic Cr precipitates of spherical shape so that relaxation effects related to the interaction of the dislocation line perpendicular to the PMI were also neglected. Hence, it is important to validate whether the relaxation effects observed near the PMI using interatomic potentials still appear if the isotropic core structure in both Fe and Cr are reproduced.

In this work we apply MD simulations to study the interaction between a $\frac{1}{2}\langle 111\rangle$ screw dislocation and pure Cr precipitates in a bcc Fe matrix at various temperatures. Although the presence of Cr precipitates in a pure Fe matrix is an unrealistic case (because of the relatively high solubility limit of Cr), the results obtained from these simulations provide exclusive information about effects related to Cr precipitates only, thus avoiding possible background effects related to the Cr in solid solution. In addition, for the edge dislocation the strengthening caused by precipitates and solid solution was found to be approximately additive.[11,18] To study the interaction of a screw dislocation with a Cr precipitate, we employ two semi-empirical interatomic potentials for the Fe-Cr system, both based on the two-band model formalism.[15] The first one was developed in Ref. 15, hereafter referred to as "PO." The second potential, presently derived, is a refit of the PO potential, where the Cr-Cr and Fe-Cr parts were fitted to especially account for (among many other properties—see Appendix for details) the dislocation core structure in pure Cr (using the most recent DFT data, not available at the time when the PO potential was developed), and is referred to as "GB." In addition, the two potentials are based on slightly different Fe components, namely, PO uses the one from Ref. 19, whereas GB uses "potential 2" from Ref. 20.

## II. SIMULATION TECHNIQUE

The model used for the simulations is based on that developed for the screw dislocation in Ref. 21. The principal axes $x$, $y$, and $z$ of the MD cell of the bcc crystal were oriented along the $[\bar{1}\bar{1}2]$, $[1\bar{1}0]$, and $[111]$ directions, respectively. Periodic boundary conditions were imposed along $z$ and an initially straight screw dislocation with left-handed thread and Burgers vector $\boldsymbol{b}=\frac{1}{2}[111]$ was created in this direction, as shown schematically in Fig. 1. The model was divided along the $y$ direction into three blocks of atoms. Those in the central region were free to move in the MD cycle, whereas those in the upper and lower blocks were held rigidly in their original positions with respect to their neighbors in the same block. A shear strain $e_{yz}$ to induce dislocation glide was then applied by simultaneous displacement of the upper and lower blocks in the $z$ direction. This resulted in a force per unit length $F=\tau b$ in the $-x$ direction for glide of the left-handed screw dislocation on the $(1\bar{1}0)$ plane (see Fig. 1). The applied shear stress $\tau$ was calculated from the force exerted on the blocks by the atoms in the central free region.

The size of the inner region was $21\times 7.5\times 20$ nm along $x$, $y$, and $z$, respectively; and it contained about $0.25\times 10^6$ atoms. In some of the simulations the length of the dislocation was increased up to 40 nm. Strain was applied at a constant rate $\dot{\varepsilon}=3.43\times 10^7\ \mathrm{s}^{-1}$ to atomic configurations previously equilibrated at temperature, $T=300$ or 600 K. The equilibrium lattice unit was also adjusted depending on the

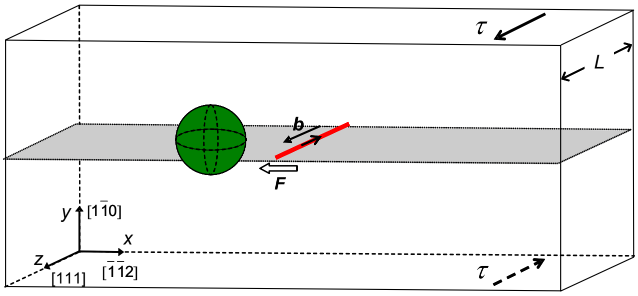

FIG. 1. (Color online) Geometry of the interaction considered. The sketch illustrates the position of the precipitate before the interaction with the left-handed screw dislocation line with $\boldsymbol{b}=\frac{1}{2}[111]$. The glide plane of the screw dislocation is $(1\bar{1}0)$ and it moves in the $[11\bar{2}]$ direction under applied shear stress $\tau$, imposed by straining an upper and lower parts of the sample. The direction of shearing is shown by the arrows near symbol "$\tau$."

ambient temperature to account for the thermal dilation. The steady state velocity, $v_D$, of a dislocation on its own at the applied strain rate is estimated from the Orowan relation $\dot{\varepsilon}=\rho_D b v_D$ for the dislocation density $\rho_D=6.5\times 10^{15}\ \text{m}^{-2}$ to be 21 m s$^{-1}$. The integration of Newton's equations was performed using a constant time step of 5 fs. All calculations were performed in the microcanonical ensemble and $T$ was monitored to confirm that additional temperature control was not required. All simulations were performed on the blue gene supercomputer at EDF.

Details of the visualization analysis used to characterize the interaction mechanisms can be found in Ref. 22. In short, atoms belonging to the dislocation core were identified using a combination of atomic properties, such as the atomic disregistry (Vitek's analysis), a common neighbor count and a potential energy threshold. A nearly spherical pure coherent Cr precipitate containing 339 Cr atoms (i.e., 2 nm diameter) was created in the MD simulation box so that its center coincided with the dislocation glide plane, as illustrated in Fig. 1.

In the course of the development of a new Cr-Cr interatomic potential (see Appendix) we have also performed some DFT calculations. The latter were done using the ultrasoft pseudopotential method (USPP) of Vanderbildt[23] and the more rigorous projector augmented wave method (PAW),[24] both implemented in the Vienna *ab initio* simulation package (VASP).[25] The generalized gradient approximation (GGA) of Perdew and Wang[26] has been used. The relaxation of supercells was performed with 125 $k$ points sampling, following the convergence tests. The plane wave cut off for the USPP and PAW calculations was at 300 eV. All relaxations were performed under constant volume conditions. The USPP method was used for the calculation of the excess stacking fault energy and the PAW method for the study of the screw dislocation core structure. Nonmagnetic bcc Cr was considered in both cases.

To calculate the excess stacking fault energy for a given fault plane and vector, a rigid translation of two crystal blocks surrounding the fault plane is applied, as was done in Ref. 27. The atoms were relaxed only in the direction perpendicular to the fault plane [(110) or (112)] to reach the convergence of forces with the criterion 0.02 eV/Å. Free surfaces parallel to the fault plane and periodic boundary conditions in the remaining directions were used in order to investigate all possible fault planes and vectors.

To simulate a $\frac{1}{2}\langle 111\rangle$ screw dislocation, the dislocation line was placed in the center of a bcc supercell containing a stacking of three (111) atomic planes. An initial atomic displacement field derived from linear isotropic elasticity was then applied. The atoms belonging to the outer shell (surrounded by vacuum) were fixed in their positions and the atoms in the inner block surrounding the dislocation core were relaxed. A periodic boundary condition was applied along the dislocation line. A DFT supercell containing 192 atoms was used with a Monkhorst-Pack $1\times 1\times 4$ $k$-point grid to sample the Brillouin zone.

## III. RESULTS AND DISCUSSION

The PO potential has already been intensively exploited to study primary damage,[28] migration of point defects and their clusters[29–31] and also properties of both edge and screw dislocations[11,14,32,33] in Fe-Cr alloys of different content. Its major drawbacks are (i) symmetrical heat of mixing for random Fe-Cr alloys and (ii) degenerate core structure for a $\frac{1}{2}\langle 111\rangle$ screw dislocation in pure Cr. The latter is particularly important when evaluating the reliability of the results obtained from simulations of the dislocation-precipitate interaction. The newer potential was developed especially to solve the mentioned problems. Before presenting the results on the dislocation-precipitate interaction we show some benchmark calculations, done with the new potential for the comparison with the DFT data reported in Ref. 17.

### A. Benchmark of the applied interatomic potentials

First, let us compare the properties of edge and screw dislocations as predicted by the two potentials. The core energy and radius, shear modulus, Poisson ratio, and Peierls stress calculated following Ref. 11 for a $\frac{1}{2}\langle 111\rangle$ screw and $\frac{1}{2}\langle 111\rangle\{110\}$ edge dislocation in the pure metals are summarized in Table I. Clearly, the two Fe-Fe potentials provide very similar results, whereas the Cr-Cr potentials exhibit at least two essential differences. The shear modulus for the GB potential is about 30% smaller, while the Poisson ratio is twice larger than the corresponding value for the PO potential. The difference of shear moduli can be clearly seen in Fig. 2(a) that shows the stress-strain curves of crystals containing a $\frac{1}{2}\langle 111\rangle$ screw dislocation. The crystals were sheared in the $(1\bar{1}0)$ plane in the [111] direction by increasing the strain in increments of $10^{-5}$. The induced stress was measured after relaxation at each step, performed using MS techniques. Interestingly, the two Cr-Cr potentials predict approximately the same Peierls stress ($\tau_P$), which is higher than $\tau_P$ for Fe by 35% and 55% according to the PO and GB potentials, respectively. According to the AR method, the difference is 35%.[17]

Furthermore, we have estimated the variation of the crystal energy while an atomic row is displaced along a $\langle 111\rangle$ direction in the same manner as was done in Ref. 17. These

TABLE I. Properties of Fe and Cr as obtained from the interatomic potentials.

| Value, unit/Material | Iron | | Chromium | |
|---|---|---|---|---|
| Potential set | PO | GB | PO | GB |
| Lattice unit $a_0$ (nm) | 0.28553 | 0.28553 | 0.2878 | 0.2866 |
| Core radius $r_0,b$ | 3 | 3 | 3 | 3 |
| Core energy $E_C$ screw (eV/nm) | 4.24 | 4.27 | 6.27 | 6.23 |
| Core energy $E_C$ edge (eV/nm) | 6.97 | 7.01 | 9.71 | 9.6 |
| Shear modulus[a] $\mu$ (GPa) | 73 | 73 | 130 | 89 |
| Poisson[b] ratio $v$ | 0.49 | 0.49 | 0.21 | 0.4 |
| Peierls stress for $\frac{1}{2}\langle 111\rangle$ screw dislocation (GPa) | 1.4 | 1.3 | 1.95 | 2.02 |

[a] Shear modulus estimated by straining a crystal on a $\{110\}$ plane in a $\langle 111\rangle$ direction, as was done in Ref. 52.

[b] Poisson ratio was determined following the method used in Ref. 53 for pure Fe.

results are presented in Figs. 2(b) and 2(c) and compared to the data from Ref. 17. According to the AR method, the energy curve exhibits a double hump for both Fe and Cr, but the curve for Cr lays well above the Fe one. The latter is reproduced by both potentials, but the double hump structure is found only for Fe [see Fig. 2(b)]. Yet, the GB potential provides a shape of the curve closest to the one obtained with the AR method. According to both potentials [see Fig. 2(c)] the displacement of a Cr row in an Fe matrix leads to a reduction in the height of the energy barrier, in agreement with the AR method.[17] Thus isolated Cr atoms are expected to facilitate the shear process between Fe-Cr rows.

Second, we have repeated the calculations of the core structure and polarizability of the dislocation interacting with a single Cr atomic row, a pair of Cr atomic row and a cluster containing three Cr atomic rows. The differential displacement maps obtained using the GB potential are shown in Fig. 3, together with the polarizability calculated as[34]

$$p = \frac{|d_{AB} - d_{BC}| + |d_{CD} - d_{DE}| + |d_{EF} - d_{FA}|}{b}. \tag{1}$$

Here, $d_{ij}$ ($i,j = A$, $B$, $C$, $D$, $E$, or $F$) is the relative displacement between two neighboring atoms in the two columns denoted as $i$ and $j$ (see Fig. 3). The data reported in Ref. 17 are given in parenthesis and it corresponds well to the results obtained with the GB and PO potentials (not shown here).

We thus conclude that the benchmark calculations show satisfactory agreement with the data obtained by the DFT parameterized AR method. In what follows we describe the interaction of a $\frac{1}{2}\langle 111\rangle$ screw dislocation with a Cr precipitate.

### B. Interaction of a Cr precipitate with a $\frac{1}{2}\langle 111\rangle$ screw dislocation

#### *Analysis of the dislocation movement*

MD simulations performed in pure Fe show that the screw dislocation glides in the $(1\bar{1}0)$ plane at $T=300$ and 600 K in the conditions specified in Sec. II. The motion of the screw dislocation proceeds via the nucleation of kink pairs and their propagation along the dislocation line. Within MD loading conditions the velocity of the dislocation is thus controlled by the rate of nucleation of kink pairs. This is a probabilistic event determined by the stress-temperature state and dislocation line length.[35] Each successful nucleation event results in the displacement of the dislocation and decrease of the resolved stress determined by the amount of slip produced by the dislocation. Hence, a typical stress-strain curve, such as the one shown in Fig. 4, consists of a set of irregular sawlike peaks, whose height and interspacing fluctuate.[35] To see the relation between the stress state and dislocation movement we displayed the evolution of the dislocation core position, determined by averaging over the whole dislocation line, in the (111) plane. The evolution along the $[\bar{1}\bar{1}2]-X$ direction gives information about the advance of the dislocation core in the $(1\bar{1}0)$ glide plane, while the evolution along the $[1\bar{1}0]-Y$ direction determines the cross-slip movement. Thus, if the dislocation glides in the $(1\bar{1}0)$ plane without cross-slip, the $Y$ coordinate stays constant and the $X$ coordinate exhibits steplike drops (with a height of $\sqrt{6}/3a_0$—distance between two Peierls valleys in a bcc lattice), as shown in Fig. 4. Clearly, each drop of the stress must result in the advance of the dislocation core position. In the following we also apply these type of diagrams to describe the dislocation-precipitate interaction.

### C. Interaction mechanism at elevated temperature

Consider the loading diagram shown in Fig. 5(a) for the dislocation interacting with a 2 nm precipitate at $T=600$ K, modeled using the PO potential. The interaction process can be described as follows. The dislocation moves toward the precipitate and the resolved stress constantly increases, which suggests that the interaction is repulsive. This is consistent with an excess in shear modulus of about 60 GPa for this interatomic potential. As soon as the dislocation reaches the PMI, indicated by the dashed line in Fig. 5(a), it starts to curve around the precipitate. The atom-core visualization of the curved dislocation is presented in Fig. 6(a). When the resolved stress reaches 400 MPa the dislocation penetrates the precipitate and after making a few successive jumps it gets blocked again, but now inside the precipitate. Note that according to the shear modulus misfit model, it is energeti-

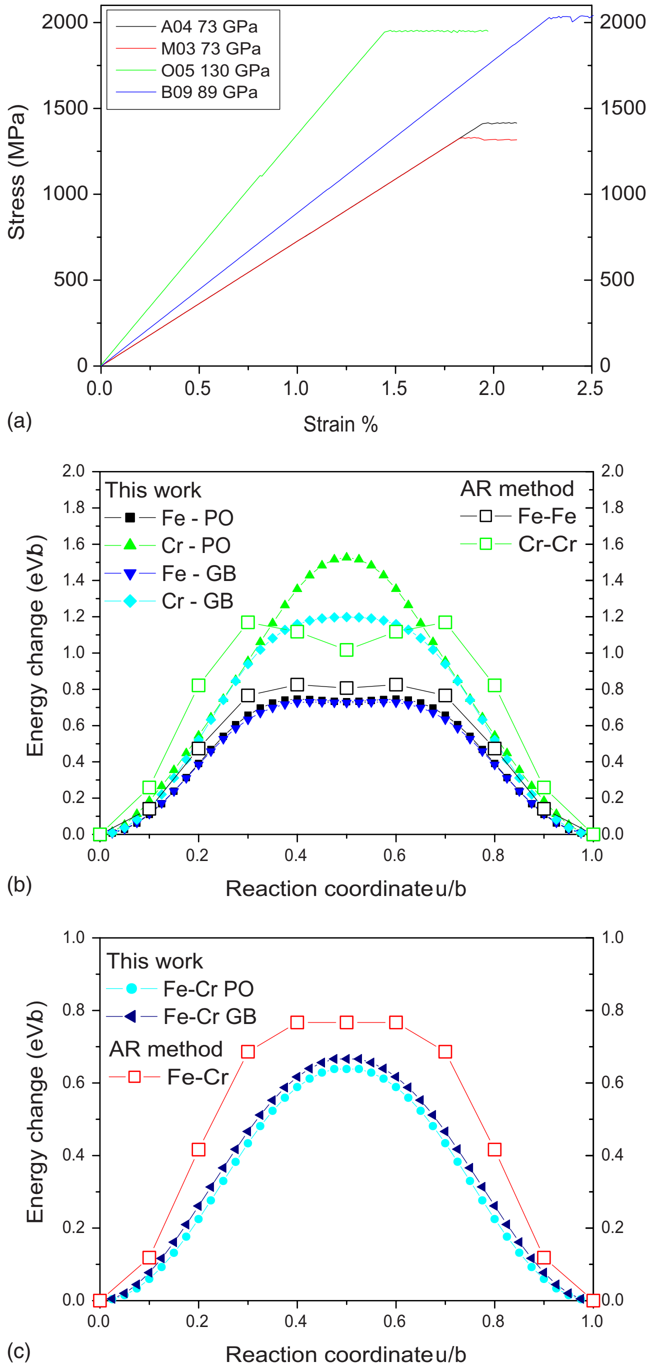

FIG. 2. (Color online) (a) Stress-strain relationship for a $\frac{1}{2}\langle 111\rangle$ screw dislocation gliding on a $(1\bar{1}0)$ plane, computed with MS techniques, for the several pure species potentials employed. Variation in the energy versus normalized atomic row displacement $\boldsymbol{u}/\boldsymbol{b}$ along a $\langle 111\rangle$ direction for (b) pure metals and (c) Fe-Cr calculated using the PO and GB potentials and compared with the data from Ref. 17.

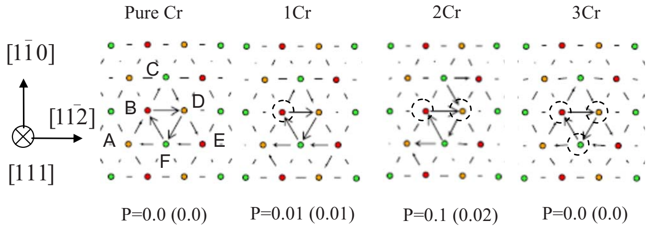

FIG. 3. (Color online) Polarization of the screw dislocation core, defined in Eq. (1), as a function of a number of solute atomic rows located in the dislocation core, calculated using the GB potential and AR approach (data given in brackets, taken from Ref. 17).

cally favorable to pinch off the dislocation from the precipitate; yet it does not happen immediately, contrary to the case of the edge dislocation.[11] This shows that the friction stress inside the precipitate is still high, even at 600 K. After applying a substantial load (of 1.2%) which results in a resolved stress of ~410 MPa, the dislocation leaves the precipitate, as shown in the loading diagram in Fig. 5(a). The dislocation line configuration at the critical stress is shown in Fig. 6(b). Since the dislocation glided through the precipitate, the latter was sheared at its equator. As can be seen from Fig. 5(a), no cross-slip events occur during the whole interaction process. Although the maximum resolved stress was registered at the moment the dislocation releases from the precipitate, the stress at which the penetration occurs is only 10 MPa lower.

When the GB potential was applied with the same simulation conditions [see loading diagram in Fig. 5(b)], two cross-slip events occurred while the dislocation was moving inside the precipitate. First the dislocation core lifted up and then moved down, back to the original glide plane. A careful inspection of the atom-core analysis revealed that the cross-slip events occurred due to the emission of kinks at the PMI. It should also be noted that the maximum resolved stress (350 MPa) is considerably lower than that registered in the simulation with the PO potential. The main difference between the two simulations is that with the GB potential, the critical stress is reached at the penetration moment. On the one hand, the lower penetration stress obtained with the GB model is consistent with the lower shear modulus misfit. On the other hand, one may also expect that the penetration of the dislocation and its movement inside the precipitate proceeds at a higher stress with the PO potential, due to the isotropic-to-degenerate core structure transformation. Therefore, the dislocation movement requires the constriction of the core into a compact one.

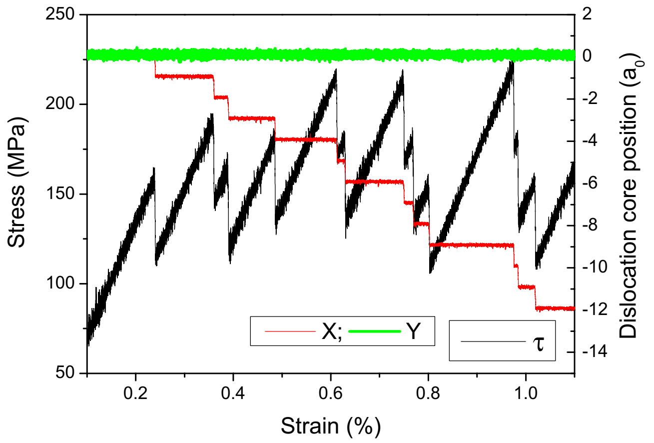

FIG. 4. (Color online) Evolution of the resolved shear stress and position of the dislocation core versus applied strain for the dislocation in pure bcc Fe at 300 K.

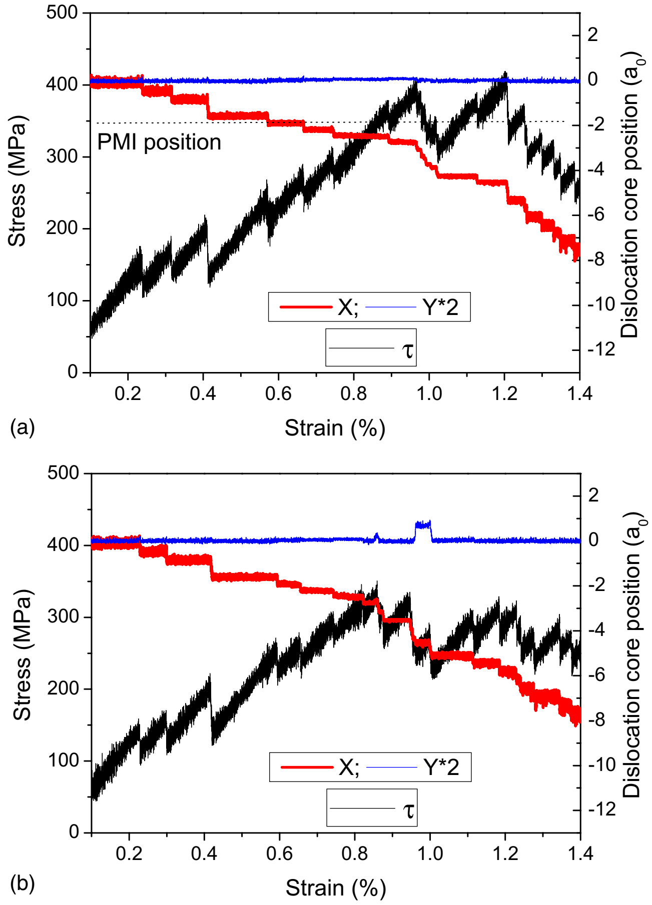

FIG. 5. (Color online) Evolution of the resolved shear stress and position of the dislocation core versus applied strain for the dislocation in pure bcc Fe simulated at $T=600$ K with the (a) PO and (b) GB potentials. The position of the PMI interface is shown by the dashed line on (a), also note the Y coordinate is doubled for better appreciation.

### D. Interaction mechanism at room temperature

The simulations performed at $T=600$ K have shown that there is an effect of interatomic potential on the critical stress but no essential difference concerning the interaction mechanism. When the same simulations were repeated at $T=300$ K, a completely different interaction mechanism was found. Consider the loading diagrams presented in Fig. 7. The beginning of the interaction process is the same with both potentials and the stress increases while the dislocation approaches the PMI. However, for the PO model, at the moment the dislocation reaches the PMI it starts to cross-slip downward in the inclined $(0\bar{1}1)$ plane across the precipitate surface. The cross-slip movement can be seen clearly in Fig. 7(a) from the evolution of the *Y* coordinate of the dislocation core. The dislocation line moves toward the bottom of the precipitate then makes a few cross-slip jumps upwards in the $(\bar{1}01)$ plane and finally gets pinned. When the resolved stress reaches $\sim$800 MPa, the dislocation leaves the unsheared precipitate. In the following we shall refer to this mechanism as "bypass." The cross-slip events were seen to be related with the emission of kink pairs on the dislocation segments located nearby the PMI. In contrast, the simulations repeated with the GB potential showed the exact same mechanism as at $T=600$ K. The loading diagram, presented in Fig. 7(b), shows the presence of only two cross-slip events. The critical stress for unpinning was about 450 MPa, i.e., 100 MPa higher than at $T=600$ K. To illustrate the difference between the two interaction mechanisms, we display the trajectories that the dislocation followed while interacting with the precipitate in Figs. 7(c) and 7(d). Note, that there is a large difference between $\tau_C$ obtained with the PO and GB models in the simulations at 300 K, which are clearly ascribed to the difference in the interaction mechanism. The increase of the dislocation line length from $80\boldsymbol{b}$ to $160\boldsymbol{b}$ and decrease of the strain rate down to $10^6$ s$^{-1}$ did not change the interaction mechanisms for any potential and, therefore, we do not present the results of those simulations.

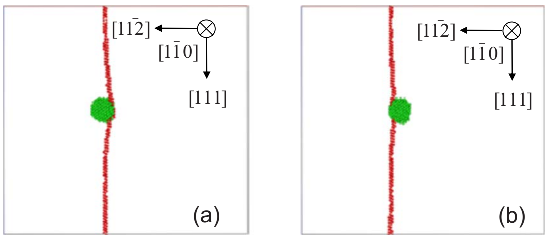

FIG. 6. (Color online) Core atom visualization of the dislocation line interacting with a 2 nm Cr precipitate, modeled with the PO potential, at the moment when the resolved shear stress reached the maximum value [the corresponding shear strain was (a) $\sim$0.95 and (b) 1.2]. The corresponding loading diagram is shown in Fig. 5(a). The dislocation moves from right to left.

### E. Analysis of the dislocation core structure in the vicinity of the precipitate surface

To reveal the reasons for the cross-slip found with the PO potential we considered MS simulations of the interaction of a screw dislocation with a 2 nm Cr precipitate. The screw dislocation was inserted in different positions along the $[11\bar{2}]$ direction in the $(1\bar{1}0)$ plane thereby emulating the glide of the dislocation through the center of the precipitate, as schematically shown in Fig. 8. Thus, the dislocation line approaches the precipitate passing states *E*, *M*, and *C*. The latter corresponds to the case when the considered dislocation segment is located in the center of the precipitate. After the dislocation is inserted in a given position, the crystal was relaxed until the energy converged to $10^{-4}$ eV/atom. The core structure of different dislocation segments, selected according to the scheme presented in Fig. 8, was calculated and the corresponding differential displacement (DD) maps were constructed.

The core structure of the segment located near the center of the precipitate (i.e., $C0$) was found to be the same as in pure Cr for the corresponding potentials i.e., the threefold split core for the PO and isotropic one for the GB potentials. The core structure of a segment penetrating the precipitate normal to its surface (i.e., $E0$) was found to be the same for both potentials. The corresponding DD maps are displayed in

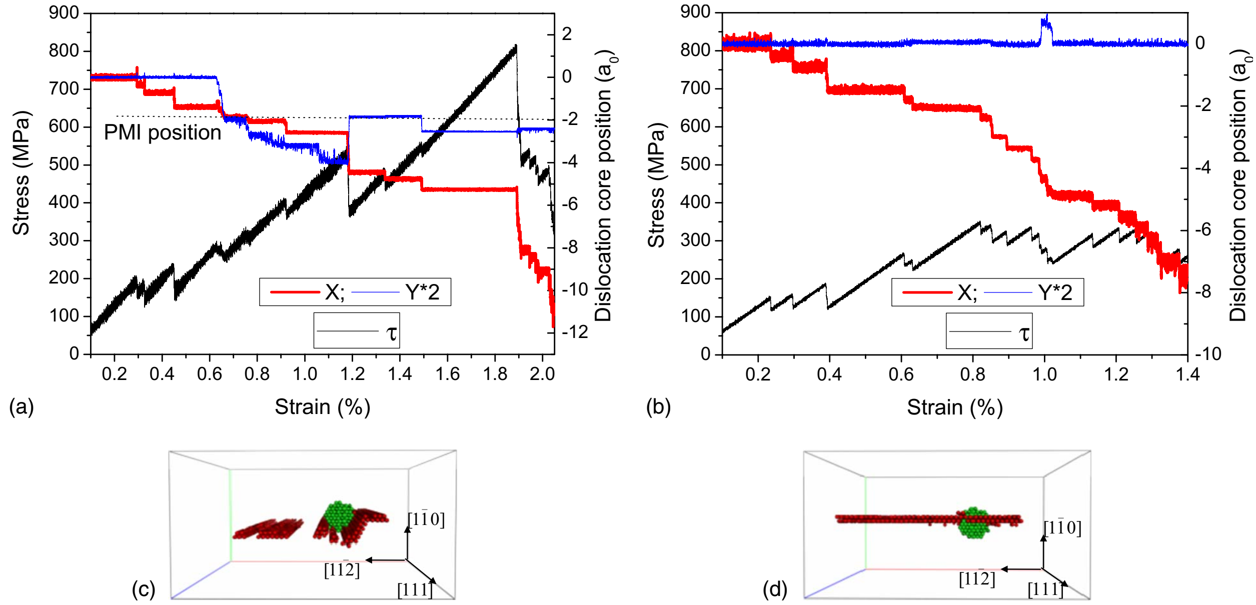

FIG. 7. (Color online) Evolution of the resolved shear stress and position of the dislocation core versus applied strain for the simulations carried at $T=300$ K with the (a) PO and (b) GB potentials. (c) and (d) show the dislocation path and position of the 2 nm precipitate, viewed in the plane perpendicular to the dislocation line i.e., (111) zone.

Table II (see row $E0$), showing a twofold structure of the core split over the precipitate surface. At the same time, the core structure of the segments penetrating the precipitate at a tangent to its surface (i.e., $M2$, $E1$, and $C2$ as the limiting case) was found to be isotropic and threefold for the GB and PO potentials, respectively (see Table II). Thus, with the PO potential, the isotropic-to-degenerate core transformation occurs not only inside the precipitate but also everywhere near the PMI. The fact that in MD simulations the cross-slip events were seen to be correlated with the formation of kinks at the precipitate surface suggests that the core transformation effect is responsible for the bypass of the dislocation under the precipitate.

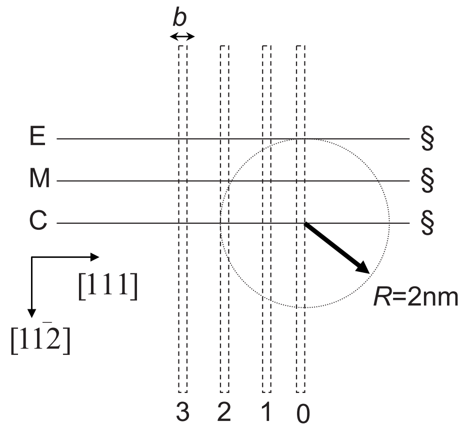

FIG. 8. Schematic picture showing the screw dislocation line (labeled as §) in the $(1\bar{1}0)$ zone approaching the center of a 2 nm precipitate passing through states E, M, and C. Different (111) cross sections (labeled as 0, 1, 2, and 3) were made to calculate the core structure.

### F. Effect of precipitate size and spacing

In this section we briefly describe the effect of precipitate size and spacing on the reaction mechanism and unpinning stress. With the PO potential, the so-called 'bypass' mechanism prevails at $T=450$ and 300 K for the dislocation (with $L=80\boldsymbol{b}$ and $160\boldsymbol{b}$) interacting with precipitates of size 1 and 2 nm. When modeling the same reactions with the GB potential, the dislocation was seen to shear precipitates in all cases. We believe that the results obtained with the GB potential are *a priori* more reliable (because of the modified Cr-Cr potential) and therefore discuss numerical data generated with this model only. The variation of the critical stress depending on the precipitate size ($D$) and center-to-center spacing (i.e., dislocation line length, $L$) on the unpinning stress is shown in Fig. 9. All reactions were performed at $T=300$ K, varying $D$ from 1 to 4 nm and $L$ from 10 to 40 nm. As expected, $\tau_C$ increases with $D$ and deceases with $L$. However, the increase of $\tau_C$ with precipitate size is much stronger than the increase due to precipitate density (determined here by the precipitate spacing). The latter result stems from the fact that in the applied loading conditions, typical for any similar type of MD simulations, the dislocation moves in the so-called single kink pair regime.[36] As a result, the dislocation line is not flexible enough for a significant curvature to occur before the penetration into the precipitate. Thus, the line tension concept is not applicable in the case of the present simulations. With this respect, we note that the results of the current MD simulations cannot be used straightforwardly to obtain the strength of Cr precipitates as a function of temperature relevant for the typical loading rates applied in mechanical tests.

## IV. SUMMARY AND CONCLUSIVE REMARKS

To summarize, we have performed a set of comparative MS and MD simulations to reveal details of the interaction

TABLE II. (Color online) Differential displacement maps drawn in the (111) zone, labeled according to the notation used in Fig. 8 and calculated after MS relaxation, for the screw dislocation interacting with a 2 nm precipitate. The fat dashed line shows the edge of the precipitate. A double arrow shows the directions of the preferential split of the core. The center of the dislocation core is shown by the symbol §.

| Configuration/ Potential | PO | GB |
|---|---|---|
| *E0* | 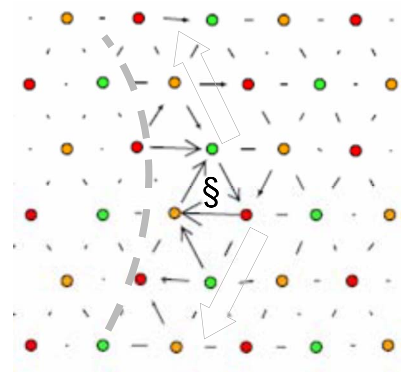 | 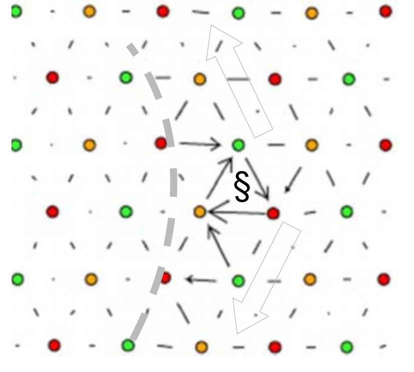 |
| *M2* | 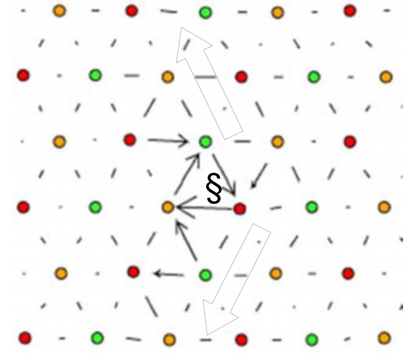 | 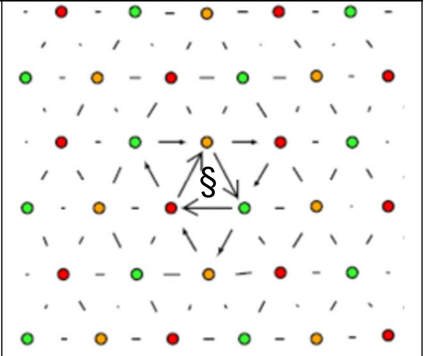 |
| *C2* | 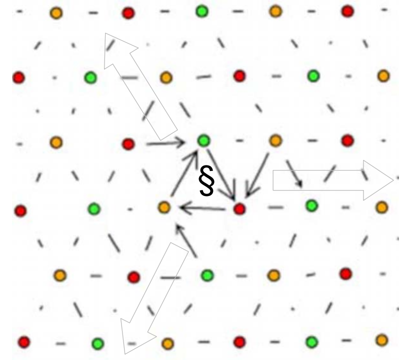 | 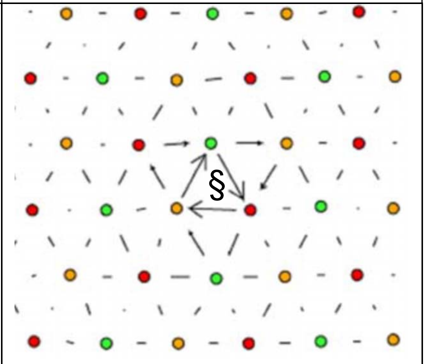 |

of a $\frac{1}{2}\langle 111\rangle$ screw dislocation with a pure Cr precipitate in bcc Fe. To perform the simulations, we have employed the two band model potential for Fe-Cr (Ref. 15) and its refitted version presented here. One of the main reasons to refit the original potential was the incorrect description of the core structure of the screw dislocation in pure Cr. The newly developed set of potentials predicts an isotropic core structure in both pure Fe and Cr.

Benchmark calculations for the core structure of the dislocation interacting with a single, pair and triple rows of Cr atoms have shown that the refitted potential provides very close agreement to the results obtained with the AR method parameterized using DFT data.[17] In particular, the core structure, polarizability and dislocation properties in pure metals are adequately described in comparison with the AR method. The main discrepancy between both potentials and the AR method was found to be the profile of the potential energy variation versus displacement of a $\langle 111\rangle$ atomic row. In contrast to the AR method, the potentials do not predict the double hump structure. However, we note that this feature can be solved by modifying only the short-range pairwise term of the potential, as was recently shown.[37]

The results of MD simulations have shown that depending on temperature, the mechanism of the interaction of the screw dislocation with a Cr precipitate and the corresponding critical stress may differ from one model to another. Two principally different interaction mechanisms were revealed. These can be described as follows: (i) the dislocation glides in the $(1\bar{1}0)$ plane cutting the precipitate and (ii) the dislocation bypasses the precipitate without shearing it by changing

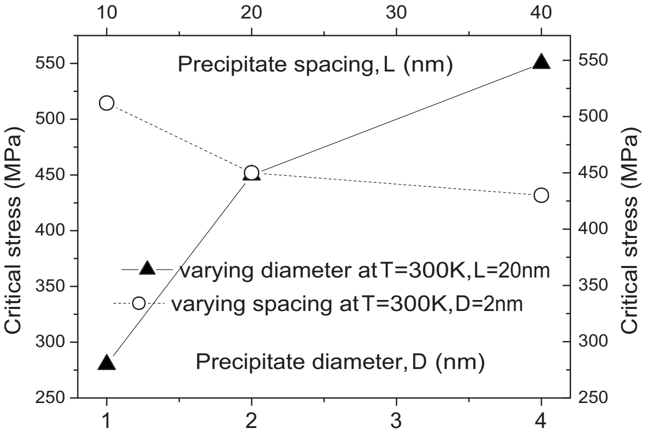

FIG. 9. $\tau_C$ as a function of the precipitate size and center-to-center spacing. Simulations are performed at $T=300$ K using the GB potential.

the glide plane from the $(1\bar{1}0)$ to $(0\bar{1}1)$, moving over the precipitate surface downwards to the bottom of the precipitate and then upwards (see Sec. III B for details). After the dislocation is unpinned from the "precipitate's south pole" it continues to glide in the $(1\bar{1}0)$ plane. The latter mechanism appeared in simulations performed at room temperature with the PO potential, whereas the former one in all other cases. Both potentials predict similar $\Delta\tau_P$ for a $\frac{1}{2}\langle 111\rangle$ screw dislocation in Fe and Cr but different core structures in Cr. The critical stress for the unpinning of a dislocation from a Cr precipitate, considering the shearing mechanism, is higher for the PO potential, consistent with the isotropic-to-degenerate core transformation occurring with this potential. If the interaction results in the bypass, the critical stress increases drastically (at least doubles). From the view point of the dislocation core structure, the results obtained with the refitted potential should be considered as more reliable.

The reason for the glide of the dislocation in a $\{112\}$ plane around the precipitate, seen with the PO potential, is most likely the isotropic-to-degenerate core transformation occurring at the moment when the dislocation penetrates into the precipitate (see Sec. III C for details). The core of the dislocation segment located in the immediate vicinity of the PMI was found to be essentially spread in the two $\{110\}$ planes inclined to the dislocation glide plane. The strain field created by the precipitate can be responsible for the spread of the non-degenerate core outside the precipitate region,[14] as was found using the PO potential. Such a spread was not seen with the GB potential, predicting a compact core for the dislocation segments located near the PMI as well as inside and outside the precipitate. Thus, the core structure modification seems to be responsible for the bypass mechanism. In addition, this effect was found to be insensitive to a change of the dislocation line length or strain rate, suggesting that preferential emission of kinks near the PMI triggers the bypass mechanism. Yet, we cannot explain why the interaction mechanism involving stable glide activates once the temperature is raised to 600 K or above. More involved studies of the effects of temperature, precipitate size, dislocation length and applied strain rate on the interaction mechanism and unpinning stress as well as the rationalization of the features of the potential governing the bypass mechanism around the precipitate will be addressed in a future work.

## ACKNOWLEDGMENTS

We thank Chen for providing numerical data from Ref. 17. R.C.P. wishes to acknowledge partial support from CONICET-PIP 5062 and UNSAM-C057. This work has been partially supported by the European Commission within the project GETMAT under Grant No. FP7-212175. D.T. also acknowledges the financial support provided by COST within mission Grant No. COST-STSM-P19-4682.

## APPENDIX: DEVELOPMENT OF Fe-Cr AND Cr-Cr POTENTIALS

In this appendix we provide the formalism and parameterization of our newly developed potential (GB) and compare its properties of interest for our study to the PO one. A more detailed account will be published elsewhere.[38]

Within the 2BM formalism[15] in which the GB and PO potentials are developed the total energy is given as the EAM energy with an extra embedding term,

$$E = \frac{1}{2}\sum_{i,j(i\neq j)} V_{t_i t_j}(r_{ij}) + \sum_i F^d_{t_i}(\rho^d_i) + \sum_i F^s_{t_i}(\rho^s_i). \qquad \text{(A1)}$$

Here $V$ denotes the pair interaction, $F^d$ is the EAM embedding term (due to the $d$-band electrons), $F^s$ is an extra embedding term due to the $s$-band electrons, and $t_i$ stands for the atom type (in our case Fe or Cr) on site $i$. The electron densities, $\rho^d$ and $\rho^s$, for the $d$- and $s$-band, respectively, are calculated as

$$\rho^\lambda_i = \sum_{j(j\neq i)} \varphi^\lambda_{t_i t_j}(r_{ij}). \qquad \text{(A2)}$$

Here $\varphi^d$ and $\varphi^s$ are the $d$- and $s$-density functions, respectively, which comply with the relations,

$$\begin{cases} \varphi^d_{AA} = \varphi^d_{BA} = \varphi^d_A \\ \varphi^d_{BB} = \varphi^d_{AB} = \varphi^d_B \\ \varphi^s_{AA} = \varphi^s_{BB} = 0 \\ \varphi^s_{AB} = \varphi^s_{BA} \end{cases}. \qquad \text{(A3)}$$

With this choice, the $d$-density reduces to the EAM density, and the $s$-density samples the local concentration[39] so that it is only relevant to the alloy, not contributing to the pure elements' energy. Tabulations of all the potential functions containing up to 5000 points are available online (http://www.ctcms.nist.gov/potentials/) or upon request to the authors. The tables are also available as supplementary materials for this manuscript. The $s$-embedding functions are given by $F^s_{\mathrm{Fe}} = -0.217\,009\,784\sqrt{\rho} + 0.388\,002\,579\rho^2$ and $F^s_{\mathrm{Cr}} = -0.009\,775\,576\,32\sqrt{\rho} + 0.374\,570\,104\rho^2$. Due to their singular slope in the origin, care should be exercised if used in tabular form.

The main differences between our and the PO potential concern the pure elements and the choice of $s$-embedding

TABLE III. Summary of the basic properties of the two Cr-Cr potentials.

| | Experiment or DFT | This Work | PO Cr |
|---|---|---|---|
| $a_0$ (Å) | 2.878[a]/2.834[b] | 2.866 | 2.878 |
| $B$ (GPa) | 208[c] | 215 | 208 |
| $C'$ (GPa) | 152[c] | 155 | 152 |
| $C_{44}$ (GPa) | 105[c] | 108 | 105 |
| $E_{\mathrm{coh}}$ (eV) | 4.10 | 4.10 | 3.84 |
| $E_{\mathrm{f}}^{\mathrm{V}}$ (eV) | $2.0\pm0.2$ [d]/2.59[b] | 2.52 | 2.56 |
| $E_{\mathrm{m}}^{\mathrm{V}}$ (eV) | 0.95[e] | 0.94 | 0.99 |
| $E_{\mathrm{coh}}^{\mathrm{bcc}}-E_{\mathrm{coh}}^{\mathrm{fcc}}$ (eV) | −0.4 [b] | −0.16 | −0.03 |
| $E_{\mathrm{f}}^{\langle 110\rangle}-E_{\mathrm{f}}^{\langle 111\rangle}$ (eV) | −0.02 [b] | −0.07 | −0.02 |
| $E_{\mathrm{f}}^{\langle 110\rangle}-E_{\mathrm{f}}^{\langle 100\rangle}$ (eV) | −1.12 [b] | −0.58 | −1.23 |

[a] Experiment, Ref. 54.
[b] DFT, Ref. 15.
[c] Experiment, Ref. 51.
[d] Experiment, Ref. 55.
[e] Experiment, Ref. 56.

functions. The functional form of the $s$-embedding terms is similar, though GB uses a species-dependent $s$-embedding function while for PO a unique function is used. As a consequence, the PO potential leads to a mixing enthalpy symmetric with composition, while it is asymmetric for the GB one, consistent with DFT data.[40–42]

Among the EAM type potentials available in the literature to describe pure Fe and capable of reproducing the $\langle 110\rangle$ self-interstitial configuration as the most stable, we considered those from Refs. 19, 20, and 43. We chose "potential 2" developed by Mendelev *et al.*[20] that has been widely used and tested. It has been demonstrated that the existing *Mendelev-type* potentials (e.g., Refs. 19 and 20) are those that succeed best at reproducing the properties of iron of interest for radiation damage studies.[44] However, of all, the one used for the GB potential is the only one for which a clear proof for the stable glide of a $\frac{1}{2}\langle 111\rangle$ screw dislocation in a $\{110\}$ plane exists in a wide range of temperatures.[21]

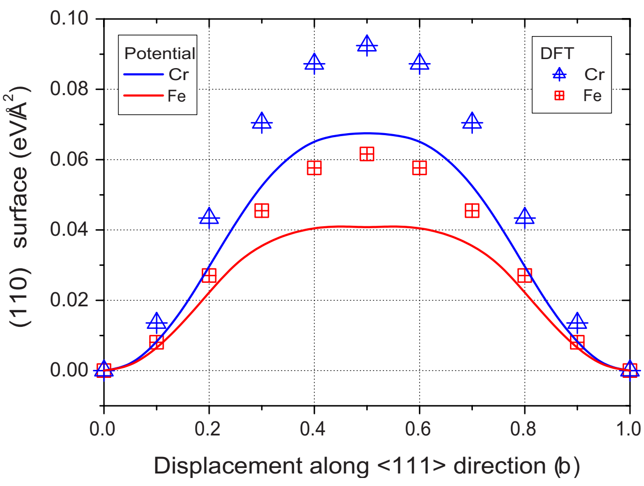

FIG. 10. (Color online) Comparison of the (110) $\langle 111\rangle$ gamma line for Fe (Ref. 20) and Cr (our potential) calculated using the potentials and DFT.

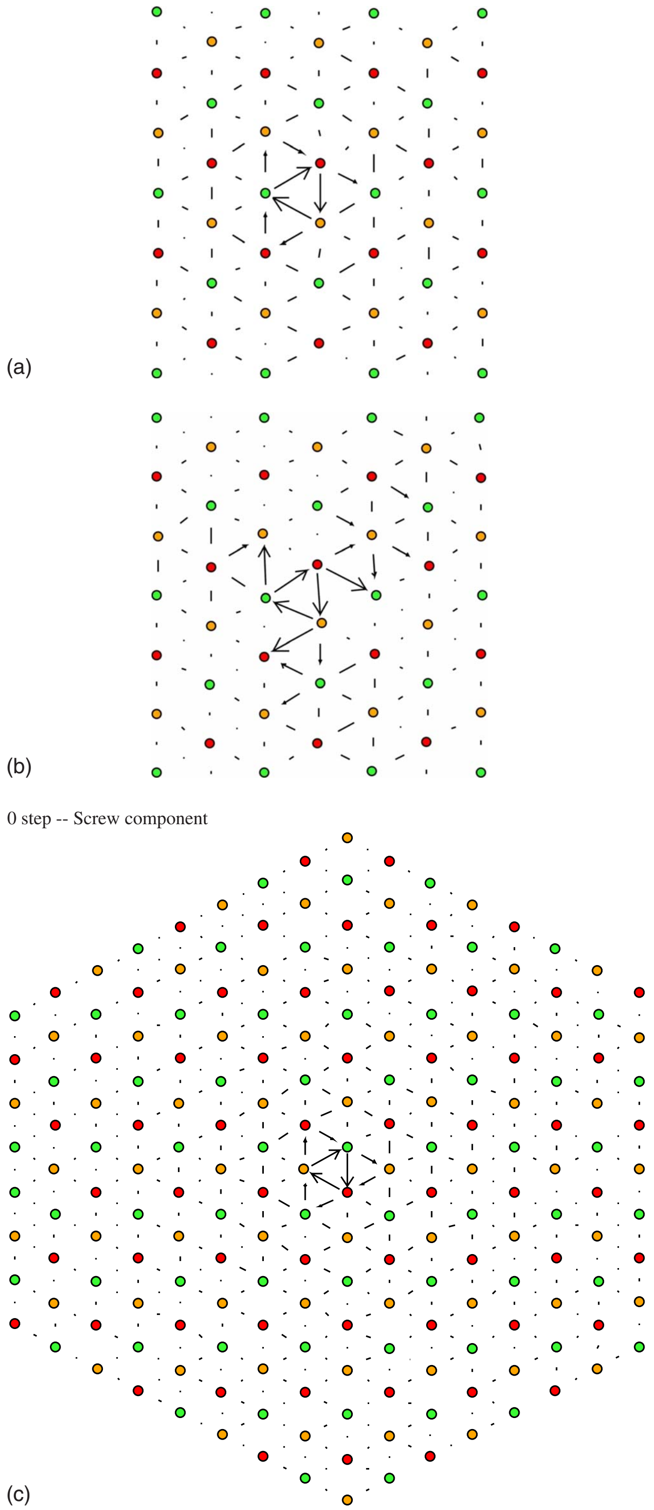

FIG. 11. (Color online) Differential displacement maps for a $\frac{1}{2}\langle 111\rangle$ screw dislocation calculated using (a) GB, (b) PO Cr-Cr potentials, and (c) DFT after relaxation.

For Cr we considered the EAM type potentials from Refs. 15 and 45. The latter was used in combination with the Fe potential,[19] to produce the PO potential. Both Cr potentials, however, suffer a drawback regarding the $\frac{1}{2}\langle 111\rangle$ screw-dislocation core structure, which has a threefold symmetry, while a compact core is predicted by DFT. For this purpose we fitted a new EAM type Cr potential, whose main properties are compared to those of the one by Olsson *et al.*[15] in Table III. In this table, $B=(C_{11}+2C_{12})/3$ is the bulk modulus, $C'=(C_{11}-C_{12})/2$ is the tetragonal shear and $C_{44}$ is the shear modulus.[46] Clearly, the experimental elastic properties are well reproduced by both potentials. Note, however, that at zero Kelvin Cr is anti-ferromagnetic and has a negative Cauchy pressure,[47] which cannot be reproduced within a standard central force framework.[48–50] Above its Néel temperature (~470 K), however, Cr is paramagnetic with a positive Cauchy pressure.[51] Since we are interested in the alloy's properties at elevated temperatures (>300 K), we fitted our Cr potential to the elastic constants of paramagnetic Cr, linearly extrapolated down to zero Kelvin (the values given in Table III) following in this choice Wallenius *et al.*[45] Furthermore, our potential also closely fits $a_0$, $E_f^V$, $E_{coh}$, and $E_m^V$, particularly the latter two. The relative stability of the different self interstitial configurations is not equally well reproduced as by the PO Cr potential, but the important features given by DFT are reproduced, i.e., the $\langle 110\rangle$ and $\langle 111\rangle$ configurations are almost degenerate and more stable than the $\langle 100\rangle$ configuration. The difference in stability between the bcc and fcc lattice is five times larger than in the case of the PO Cr potential, thereby providing an enhanced stability of the bcc lattice at high temperature. In summary, the basic properties of Cr are equally well reproduced by both potentials.

In Fig. 10 the (110) $\langle 111\rangle$ gamma line calculated using the Cr and Fe potentials used in the GB potential is compared to DFT predictions. According to DFT, the maximum for Fe is about half the one for Cr, which is also reproduced by both potentials. At the same time, both potentials underestimate the absolute value predicted by DFT by ~30%.

In Fig. 11, the differential displacement maps for the screw dislocation core in Cr for our potential and the PO Cr potential are compared, both obtained by static relaxations. The core structure obtained with DFT calculations is shown in Fig. 11(c). Clearly, the PO Cr potential shows a threefold symmetry, while for our potential the core structure is compact, as predicted by DFT. We now can summarize the main features of the newly developed Fe-Cr and Cr-Cr potentials as follows. The set of potentials predicts (i) asymmetric heat of formation for Fe-Cr, (ii) compact core structure for a $\frac{1}{2}\langle 111\rangle$ screw dislocation in Fe and Cr, (iii) correct order for the relative stability of different configurations for self-interstitial atoms in Fe and Cr—all in agreement with DFT.

---

*Corresponding author. FAX: +32-14-321216; dterenenty@sckcen.be

[1] R. Fisher, E. Dulis, and K. Carroll, Trans. AIME **197**, 690 (1953).

[2] R. Williams and H. Paxton, J. Iron Steel Inst. **185**, 358 (1957).

[3] J.-A. Andersson and B. Sundman, CALPHAD: Comput. Coupling Phase Diagrams Thermochem. **11**, 83 (1987).

[4] Y. de Carlan, A. Alamo, M. Mathon, G. Geoffroy, and A. Castaing, J. Nucl. Mater. **283-287**, 672 (2000).

[5] D. Bacon, Y. Osetsky, and D. Rodney, in *Dislocations in Solids*, edited by J. Hirth and L. Kubin (North-Holland, Amsterdam, 2009), p. 14.

[6] J. Marian, B. Wirth, R. Schaeublin, G. Odette, and J. Perlado, J. Nucl. Mater. **323**, 181 (2003).

[7] Yu. N. Osetsky, D. J. Bacon, and V. Mohles, Philos. Mag. **83**, 3623 (2003).

[8] M. Y. Lavrentiev, R. Drautz, D. Nguyen-Manh, T. P. C. Klaver, and S. L. Dudarev, Phys. Rev. B **75**, 014208 (2007).

[9] P. Erhart, A. Caro, M. Serrano de Caro, and B. Sadigh, Phys. Rev. B **77**, 134206 (2008).

[10] G. Bonny, D. Terentyev, L. Malerba, and D. Van Neck, Phys. Rev. B **79**, 104207 (2009).

[11] D. Terentyev, G. Bonny, and L. Malerba, Acta Mater. **56**, 3229 (2008).

[12] T. Harry and D. J. Bacon, Acta Mater. **50**, 195 (2002).

[13] T. Harry and D. J. Bacon, Acta Mater. **50**, 209 (2002).

[14] D. Terentyev, G. Bonny, and L. Malerba, Nucl. Instrum. Methods Phys. Res. B **267**, 3155 (2009).

[15] P. Olsson, J. Wallenius, C. Domain, K. Nordlund, and L. Malerba, Phys. Rev. B **72**, 214119 (2005).

[16] H. Suzuki, in *Fundamental Aspects of Dislocation Theory*, edited by J. Simmons, R. deWitt, and R. Bullough (National Bureau of Standards, Washington, 1970), p. 253.

[17] Z. Chen, N. Kioussis, N. Ghoniem, and T. Hasebe, Phys. Rev. B **77**, 014103 (2008).

[18] G. Bonny, D. Terentyev, and L. Malerba, J. Nucl. Mater. **385**, 278 (2009).

[19] G. J. Ackland, M. I. Mendelev, D. J. Srolovitz, S. Han, and A. V. Barashev, J. Phys.: Condens. Matter **16**, S2629 (2004).

[20] M. I. Mendelev, S. Han, D. J. Srolovitz, G. J. Ackland, D. Y. Sun, and M. Asta, Philos. Mag. **83**, 3977 (2003).

[21] C. Domain and G. Monnet, Phys. Rev. Lett. **95**, 215506 (2005).

[22] D. Terentyev, P. Grammatikopoulos, D. Bacon, and Y. Osetsky, Acta Mater. **56**, 5034 (2008).

[23] D. Vanderbilt, Phys. Rev. B **41**, 7892 (1990).

[24] G. Kresse and D. Joubert, Phys. Rev. B **59**, 1758 (1999).

[25] G. Kresse and J. Hafner, Phys. Rev. B **47**, 558 (1993).

[26] J. P. Perdew, J. A. Chevary, S. H. Vosko, K. A. Jackson, M. R. Pederson, D. J. Singh, and C. Fiolhais, Phys. Rev. B **46**, 6671 (1992).

[27] C. Domain, R. Besson, and A. Legris, Acta Mater. **50**, 3513 (2002).

[28] C. Björkas, K. Nordlund, L. Malerba, D. Terentyev, and P. Olsson, J. Nucl. Mater. **372**, 312 (2008).

[29] D. Terentyev, L. Malerba, and A. V. Barashev, Philos. Mag. Lett. **85**, 587 (2005).

[30] D. Terentyev and N. Castin, Comput. Mater. Sci. **46**, 1178 (2009).

[31] D. Terentyev, P. Olsson, T. P. C. Klaver, and L. Malerba, Comput. Mater. Sci. **43**, 1183 (2008).

[32] D. Terentyev, G. Bonny, and L. Malerba, J. Nucl. Mater. **386-388**, 257 (2009).

[33] D. Terentyev and L. Malerba, Comput. Mater. Sci. **43**, 855 (2008).

[34] G. F. Wang, A. Strachan, T. Cagin, and W. A. Goddard, Phys. Rev. B **67**, 140101(R) (2003).

[35] D. Rodney, Phys. Rev. B **76**, 144108 (2007).

[36] J. Chaussidon, M. Fivel, and D. Rodney, Acta Mater. **54**, 3407 (2006).

[37] S. Chiesa, M. R. Gilbert, S. L. Dudarev, P. M. Derlet, and H. Van Swygenhoven, Philos. Mag. **89**, 3235 (2009).

[38] G. Bonny, R. C. Pasianot, D. Terentyev, and L. Malerba (unpublished).

[39] G. Bonny, R. Pasianot, and L. Malerba, Philos. Mag. **89**, 711 (2009).

[40] P. Olsson, I. Abrikosov, L. Vitos, and J. Wallenius, J. Nucl. Mater. **321**, 84 (2003).

[41] T. P. C. Klaver, R. Drautz, and M. W. Finnis, Phys. Rev. B **74**, 094435 (2006).

[42] P. Olsson, I. Abrikosov, and J. Wallenius, Phys. Rev. B **73**, 104416 (2006).

[43] S. Dudarev and P. Derlet, J. Phys.: Condens. Matter **17**, 7097 (2005).

[44] L. Malerba, M.-C. Marinica, N. Anento, C. Björkas, H. Nguyen, C. Domain, F. Djurabekova, P. Olsson, K. Nordlund, A. Serra, D. Terentyev, F. Willaime, and C. S. Becquart, J. Nucl. Mater. (to be published).

[45] J. Wallenius, I. A. Abrikosov, R. Chakarova, C. Lagerstedt, L. Malerba, P. Olsson, V. Pontikis, N. Sandberg, and D. Terentyev, J. Nucl. Mater. **329-333**, 1175 (2004).

[46] C. Kittel, *Introduction to Solid State Physics* (Wiley, New York, 1996).

[47] H. J. van Rijn and H. L. Alberts, J. Phys. F: Met. Phys. **13**, 1559 (1983).

[48] R. Pasianot, D. Farkas, and E. J. Savino, Phys. Rev. B **43**, 6952 (1991).

[49] O. Yifang, Z. Bangwei, L. Shuzhi, and J. Zhanpeng, Z. Phys. Chem. Abt. B **101**, 161 (1996).

[50] Z. Bangwei, O. Yifang, L. Shuzhi, and J. Zhanpeng, Physica B **262**, 218 (1999).

[51] K. Katahara, M. Nimalendran, M. Manghnani, and E. Fischer, J. Phys. F: Met. Phys. **9**, 2167 (1979).

[52] Y. N. Osetsky and D. J. Bacon, Modell. Simul. Mater. Sci. Eng. **11**, 427 (2003).

[53] D. Terentyev, D. Bacon, and Y. Osetsky, J. Phys.: Condens. Matter **20**, 445007 (2008).

[54] W. Pearson, *A Handbook of Lattice Spacings and Structures of Metals and Alloys* (Pergamon Press, New York, 1958).

[55] G. Loper, L. Smedskjaer, M. Chason, and R. Siegel, in *Positron Annihilation*, edited by P. Jain (World Scientific, Singapore, 1985), p. 461.

[56] H. Schultz, Mater. Sci. Eng., A **141**, 149 (1991).